ADVANCED MATERIALS

Supporting Information

for *Adv. Mater.,* DOI: 10.1002/adma.201404772

Toward a New Generation of Electrically Controllable Hygromorphic Soft Actuators

Silvia Taccola, Francesco Greco,* Edoardo Sinibaldi, Alessio Mondini, Barbara Mazzolai, and Virgilio Mattoli**

Supporting Information

Towards a new generation of electrically controllable hygromorphic soft actuators

Silvia Taccola*, Francesco Greco*, Edoardo Sinibaldi, Alessio Mondini, Barbara Mazzolai and Virgilio Mattoli*

1. Image processing:

Images (61 px/mm resolution) of the activated samples were processed using Matlab (The Mathworks, Natick, MA, USA) software. A region-of-interest (ROI) was first defined based on the patterned length of each considered sample to approximately frame the curved beam portion (Figure S1, see also Supplementary Video 4). We then took the binary, complement ROI image, and once morphological closing was applied (to fill small gulfs that can possibly appear on the boundary of the binarized shape), we obtained the morphological skeleton of the actuator profile, i.e., the backbone curve from which to derive the curvature. In detail, we used two independent approaches by exploiting the built-in functions of (ultimate) erosion and skeletonization; in the latter case, we also pruned the backbone to minimize spurious effects potentially introduced on the ROI boundary. A circular arc was then fitted to the backbone by least squares minimization (greater than at least 50 points); the problem was formulated in terms of curvature to avoid singularities for the nearly straight beam configurations. Both of the considered methods provided approximately the same curvature results, and from their comparison, we estimated that the uncertainty in the curvature was within 2% of the maximum curvature. This methodology was also used for the transient analysis (actuator response to step voltage): after the ROI was defined for the selected video frames, it was linearly interpolated to perform a rapid semi-automatic analysis (nearly 1000 images processed in a few minutes on a common desktop PC).

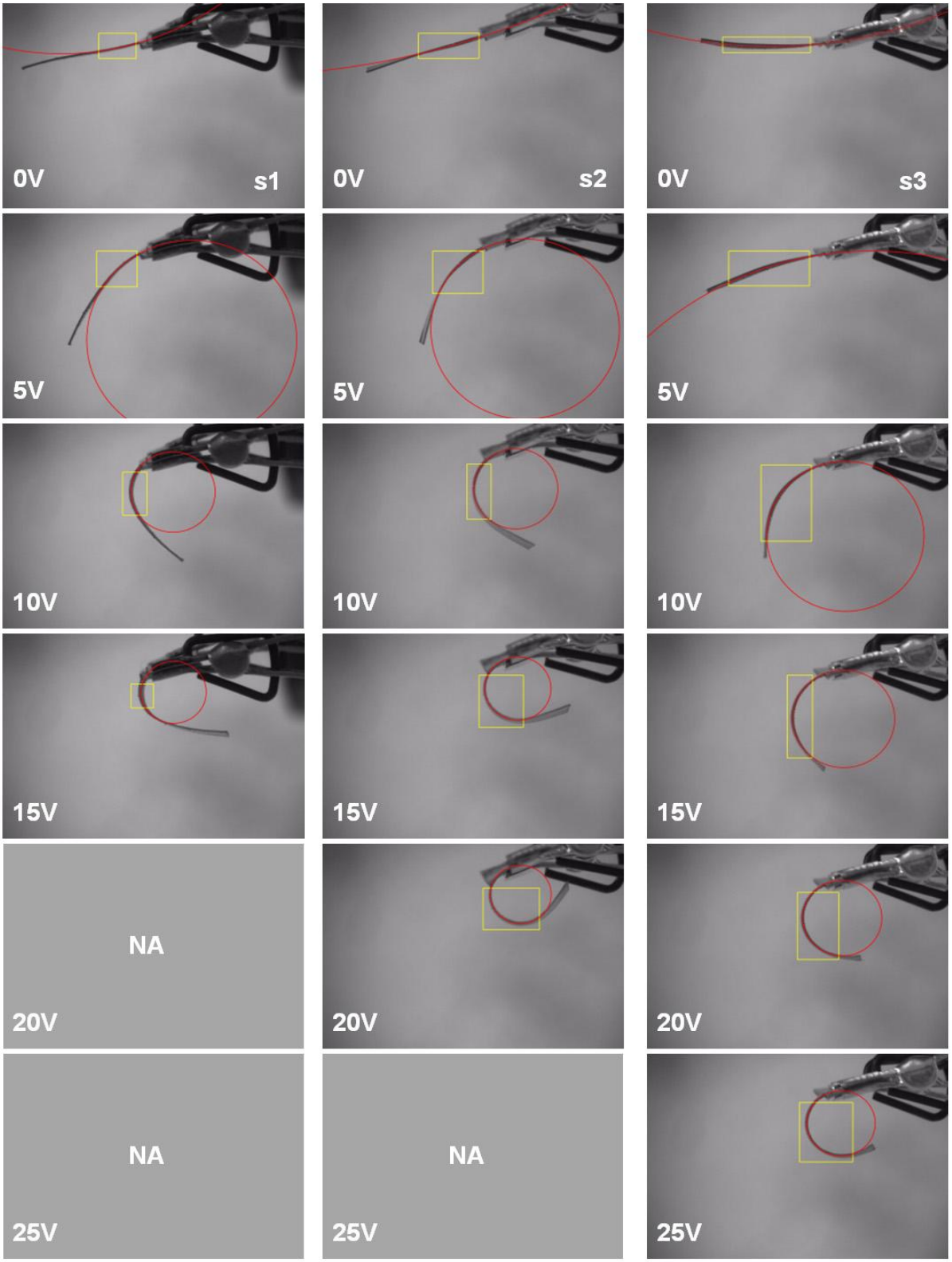

Figure S1. Actuator curvatures obtained by image processing for samples s1-3 at selected voltage. Each yellow rectangle denotes the region-of-interest (based on the patterned length) from which the corresponding curvature was extracted; the fitting circumference (red) is also shown. It can be observed that the actuator remains nearly straight closer to the tip (i.e., farther from the activated region).

2. Actuator Modeling

The static performance of the actuator was modeled using relevant expressions from linear beam theory, which was extended to a bilayer. [14] In particular, we considered the following expressions for curvature k and blocking force F_b:

$$k = \frac{\alpha}{h_s}\,\eta(m,n), \qquad \text{with} \quad \eta(m,n) \equiv m\,n\,\frac{6\,(1+m)}{1 + m\,n\,(4+6\,m+4\,m^2+m^3 n)}, \tag{S1}$$

$$F_b = E_s\,h_s^2\,\alpha\,\frac{w}{L}\,\xi(m,n), \qquad \text{with} \quad \xi(m,n) \equiv m\,n\,\frac{3\,(1+m)}{4\,(1+m\,n)}, \tag{S2}$$

where $m \equiv \frac{h_f}{h_s}$ and $n \equiv \frac{E_f}{E_s}$; h_f and E_f denote the height and the Young's modulus of the PEDOT:PSS layer (subscript f represents the active film), respectively; and h_s and E_s indicate the corresponding values for the PDMS layer (subscript s represents the passive substrate). Additionally, w and L denote the beam width and length, respectively. Finally, α represents the so-called mismatch strain, which in our case is provided by the free actuation strain of the PEDOT:PSS layer when it is not attached to the substrate. The primary underlying model assumptions that were used are the following: the beam thickness $h_f + h_s$ is small relative to the radius of curvature k^{-1} and the lateral beam dimensions (such that null stress components are assumed through the thickness); the relationship between (infinitesimal) strain and stress is linear and isotropic. Note that the curvature k is assumed to be uniform along the beam, as is the blocking torque per unit width, from which F_b is derived (also originates from the linear dependence on w in equation (S2)). We used equation (S1) and (S2) to estimate the blocking force of sample S3. In more detail, based on the experimental curvatures (see Figure 2c in main text), we first obtained α from equation (1) by adopting h_f = 600 nm, h_s = 120 µm, E_f = 1 GPa[25], and E_s = 2.28 MPa. To properly calibrate the model, and in consideration of the fact that the Young's modulus of PDMS is strongly

dependent on the crosslinking process, we experimentally measured the modulus of our PDMS samples (E_s) rather than using data taken from the literature. (see Method section on main text). Note that the obtained mismatch strains were fully consistent with the value of 2% reported in the literature.[6] We then substituted α into equation (S2), and using $w = 3$ mm and $L = 8$ mm, we predicted the corresponding blocking force, which is reported in Figure 2d (in main text) against the experimental measurements. Clearly, the model cannot be straightforwardly applied for higher curvatures, yet it remarkably matches the experimental data in the proper curvature range, thus supporting the proposed approach.

Based on the above result, we used the model to further characterize the application range of the actuator by investigating the characteristic size beyond which it might cease to be effective. In particular, we compared the blocking force obtained by equation (S2) to the actuator weight W, which was approximated as $W \approx g\,\rho_s\,h_s\,L\,w$, where g represents acceleration due to gravity and ρ_s = 960 kg m^{-3} is the density of PDMS. We thus considered the ratio $\sigma \equiv \frac{F_b}{W}$ to be a key design parameter because the bilayer must provide $\sigma > 1$ for actuation to be generally effective. After σ was observed to not depend on the beam width based on the model assumptions, we selected h_s and L as design variables; for any fixed value of h_s, we derived the maximum length $L_{\max}$ that should not be exceeded to fulfill the constraint $\sigma > \hat{\sigma}$, where $\hat{\sigma}$ is a desired threshold targeted in the design phase. Trivial algebraic passages provided the following scaling law:

$$L_{\max}(h_s) = \left(\frac{E_s\,\tilde{\alpha}}{g\,\rho_s\,\hat{\sigma}}\,h_s\,\xi(m,n) \right)^{1/2}, \qquad \text{(S3)}$$

where $\tilde{\alpha}$ is a reference value for the mismatched strain. Illustrative trends for equation (S3) are presented in Figure 2i (main text) for selected values of $\sigma = \hat{\sigma}$ (the "ultimate" boundary associated with $\hat{\sigma}$ =1 is also shown), which were obtained with $\tilde{\alpha}$ = 2% and by fixing the

remaining parameters as those from above. From this Figure, it is clear that the developed actuator is more effective for lengths that are less than approximately 1 cm. This result, which is consistent with observations during the experiments, provides a simple design criterion that complements the fact that the actuator force can be enhanced by increasing the beam width. Despite its inherent simplifications, the considered model can be suitably used for the preliminary actuator design.

3. Electrically induced bending at different humidity conditions

The electro-thermo-mechanical response of the actuators was investigated by recording the responses of the actuators to different step voltages with a digital optical microscope also in humidity controlled environment. Videos and images of the samples during the experiments were recorded with a uEye UI-2250-MM CCD camera (IDS Imaging Development Systems, Obersulm, Germany) equipped with a Zoom 6000 zoom lens (Navitar, Rochester, NY). The experiments were performed under controlled humidity conditions inside a climatic test chamber (CTC 256, Memmert). Tests have performed applying to the samples 5, 10, 15, 20, 25, and 30 V step input voltages, at different environmental humidity conditions, including 30, 40, 50, and 60% RH.

Results of the tests show that for each input voltage the bending radii of electrically activated actuators change with the RH level, due to the different equilibrium states established between the water content of the PEDOT:PSS film and the surrounding environmental humidity. This is particularly evident for low values of input voltage (see Figure S2).

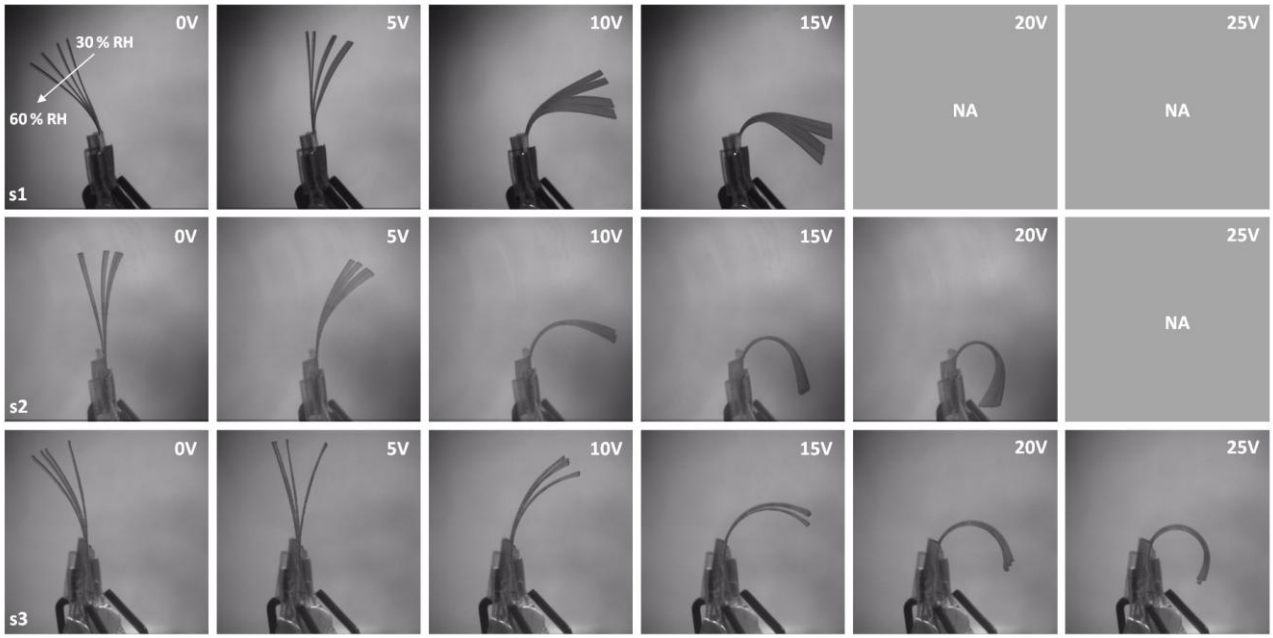

Figure S2. Effect of changes in the RH level on the electrically induced actuation of samples s1, s2, and s3. Each frame shows the superposition of the images taken at different RH levels (30, 40, 50, or 60% RH) with the arrow pointing towards the increasing RH level.

4. *Mimosa pudica* conditioning electronics

From an electronic perspective, the "artificial" *Mimosa pudica* is represented by a resistance of approximately 1 kΩ that changes slightly (but rapidly) if touched. To monitor for a possible touch, a small current is used (regulated by a dedicated variable resistor, labeled as Sense Current regulation). Small (but rapid) current variations are detected by a differentiator circuit followed by an amplifier. The output of the amplifier is collected by a microcontroller that, when triggered by a suitable pulse/signal, actuates the high-current driver (heating driver), thereby closing the leaves of the "artificial" *Mimosa pudica*. After a certain time (timing is controlled by the microcontroller system), the driver is switched-off, and the leaves return back to their initial open position. Conditioning electronic scheme of "artificial" *Mimosa pudica* is reported in Figure S3

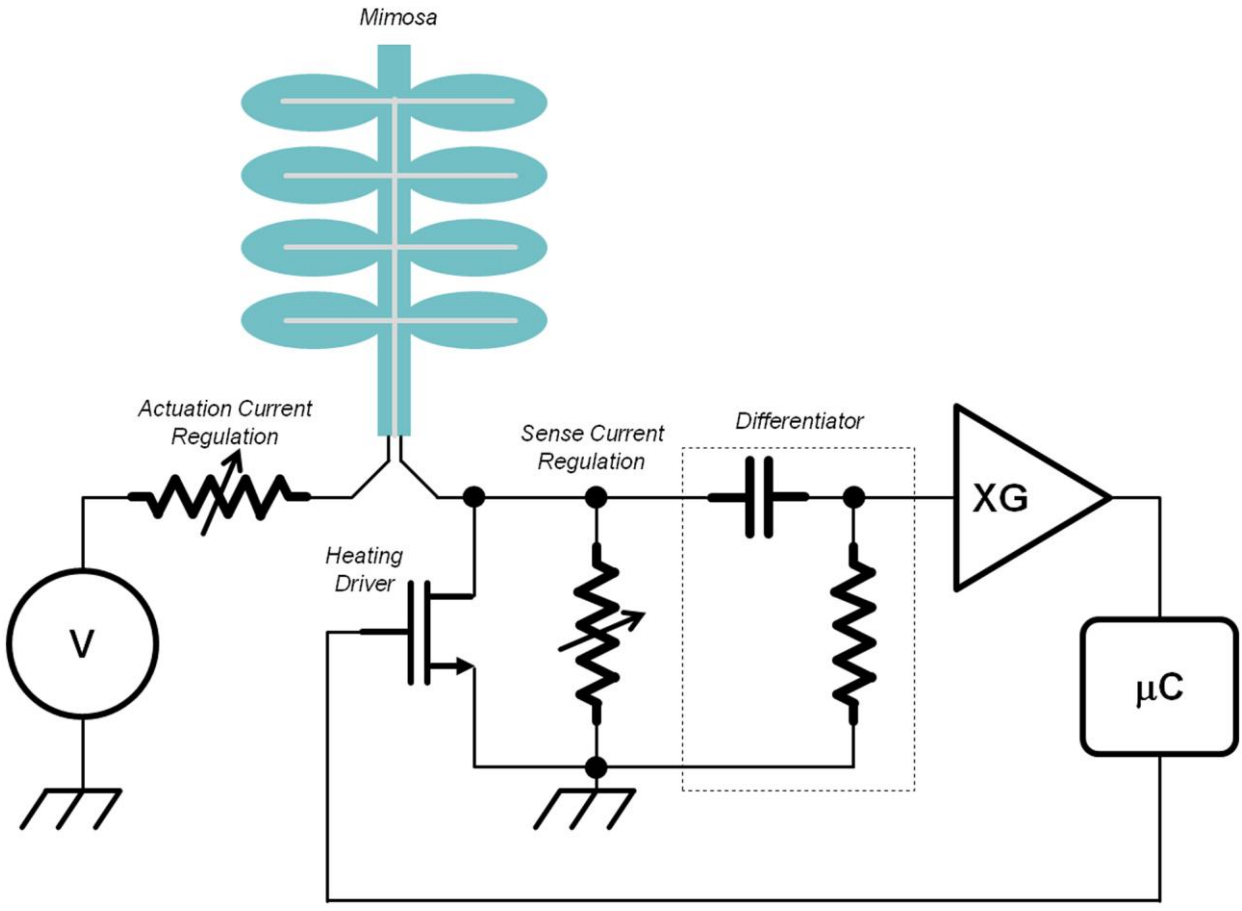

Figure S3 "Artificial" *Mimosa pudica*: conditioning electronic scheme

Video SV1: Actuator working principle

Video SV2: Overview of fabrication process

Video SV3: Active and passive actuation

Video SV4: Characterization of actuator and data extraction

Video SV5: Examples of actuation